Journal of Alloys and Compounds 782 (2019) 648–658

Contents lists available at ScienceDirect

Journal of Alloys and Compounds

journal homepage: http://www.elsevier.com/locate/jalcom

Role of the LPSO structure in the improvement of corrosion resistance of Mg-Gd-Zn-Zr alloys

Jing Liu [a, 1], Lixin Yang [b, 1], Chunyan Zhang [c], Bo Zhang [b, *], Tao Zhang [c, **], Yang Li [c], Kaiming Wu [a], Fuhui Wang [c]

[a] The State Key Laboratory of Refractories and Metallurgy, Hubei Province Key Laboratory of Systems Science in Metallurgical Process, International Research Institute for Steel Technology, Wuhan University of Science and Technology, 947 Heping Avenue, Wuhan, 430081, China
[b] Shenyang National Laboratory for Materials Science, Institute of Metal Research, Chinese Academy of Sciences, Shenyang, 110016, China
[c] Shenyang National Laboratory for Materials Science, Northeastern University, 3-11 Wenhua Road, Shenyang, 110819, China

ARTICLE INFO

Article history:
Received 26 September 2018
Received in revised form
24 November 2018
Accepted 17 December 2018
Available online 19 December 2018

Keywords:
Mg-Gd-Zn-Zr alloys
LPSO structure
Corrosion behavior
SKPFM

ABSTRACTS

The role of long period stacking ordered (LPSO) structure in the corrosion behavior of Mg-Gd-Zn-Zr alloys was investigated by means of potentiodynamic polarization experiments, hydrogen evolution tests, and microstructure characterization. The corrosion rate of the Mg-Gd-Zn-Zr alloys is mainly determined by the acceleration effect of the second phases in the micro-galvanic corrosion. After T4 heat-treatment, the β-$(Mg,Zn)_3Gd$ eutectic phase in the as-cast Mg-Gd-Zn-Zr alloys transforms into an X phase with a 14H-LPSO structure. According to the results of scanning Kelvin probe force microscopy (SKPFM), the potential difference between LPSO phase and the α-Mg matrix is 243 mV, whereas, it is 290 mV between the eutectic phase and matrix in the as-cast alloys. The low relative potential and volume fraction of the LPSO phase reduce the acceleration degree of micro-galvanic corrosion. As a result, the corrosion resistance of Mg-Gd-Zn-Zr alloys improves significantly by the LPSO structure.

1. Introduction

As the light-weight structural material, Mg alloys are commonly used in aerospace, automotive industries, electronics and automobile [1–10] for their high-specific strength, good electromagnetic shielding characteristics, and favorable casting capability [2–14]. Nevertheless, the bad resistance to creep [13] and low absolute mechanical strength [14,15], as well as the poor corrosion resistance [13–17] are three important drawbacks that hinder the widespread applications of Mg alloys [18,19]. In recent years, Mg alloys containing rare earth (RE) elements, particularly with LPSO structure, have attracted much attention due to their outstanding comprehensive mechanical properties [20–28], such as excellent tensile strength [20], superior creep resistance [21,22], high fracture toughness and good fatigue strength [23]. For example, Yamasaki [24] and Kawamura [25] reported that the tensile yield strength and elongation of the Mg-RE alloy containing LPSO structure can reach to 610 MPa and 345 MPa, and 5% and 6.9%, respectively. The effects of LPSO structure on the mechanical properties of Mg-RE alloys have been investigated extensively [28–30]. Generally, an LPSO structure is obtained mainly through heat-treatment [31–37]. During the heat-treatment, both the precipitation of LPSO structures and the grain refinement play important roles in improving the strength and creep resistance of Mg-RE alloys [4,25]. However, the phase transformation by heat-treatment is very challenging for the corrosion protection of Mg alloys, as the precipitation of the second phases during the heat-treatment is a vital factor in deciding the micro-galvanic corrosion behavior [16,17]. Therefore, several researchers have investigated the relationship between microstructure and the corrosion behavior of Mg-RE alloys with LPSO structures [37–43].

Yamasaki et al. [13,28] illustrated that the microstructure evolution leads to a change in the electrochemical behavior of Mg-Zn-Y alloys, and consequently, affects their corrosion resistance. Zhang et al. [38–40] studied the effect of microstructure on the biocorrosion behavior of Mg-Gd-Zn alloys in a simulated body fluid. They revealed that the volume fraction and distribution of LPSO structure greatly affect the corrosion behavior of Mg-RE alloys.

* Corresponding author.
** Corresponding author.
E-mail addresses: bozhang@imr.ac.cn (B. Zhang), zhangtao@mail.neu.edu.cn (T. Zhang).
[1] Equally contributed to this work.

https://doi.org/10.1016/j.jallcom.2018.12.233
0925-8388/

Meanwhile, Wang et al. [41] elucidated that the corrosion morphology and resistance of an Mg-15.24Gd-4.75Zn alloy exposed to 3.5 wt% NaCl solution depend on the LPSO phase, which not only acts as an anode during micro-galvanic corrosion but also as a corrosion barrier to corrosive ions. However, all these observations are superficial evaluations of the corrosion behavior of Mg-RE alloys, but the precise effects of LPSO structure on the corrosion properties have not yet been clarified [13,14,44]. Furthermore, there is a discrepancy between the results of different studies. Srinivasan [14,41] suggested that the LPSO phase facilitates the corrosion in Mg-Gd-Zn alloys. A higher corrosion rate observed can be related to a significant increase in the volume of the LPSO phase in the alloys. Perez et al. [45] also observed that the LPSO phase is more preferentially attacked by the corrosion ions when compared to the other intermetallic phases. In addition, both Xu [15] and Zhang [46] revealed that the increased volume fraction of LPSO phase and the distribution of LPSO structure accelerate the corrosion behavior of Mg-Zn-Y alloys due to the galvanic corrosion. In contrast, several other researchers concluded that the LPSO structure is beneficial to the improvement of the corrosion resistance of Mg-RE alloys [36–38,46–53].

In summary, all earlier studies on the corrosion behavior of Mg-RE alloys with an LPSO structure are just general characterization and lack a systematic in-depth analysis of the mechanism. Consequently, further extensive research is required to illustrate the corrosion mechanism of Mg alloys with an LPSO structure for broadening the applications of this kind of promising Mg alloys. Therefore, in this study, we first characterized the corrosion behavior of Mg-Gd-Zn-Zr alloys with and without an LPSO structure, and then, the analysis of the mechanism of the LPSO structure on the corrosion behavior was carried out systematically and extensively. Finally, an attractive conclusion was obtained that the significantly improved corrosion resistance of Mg-Gd-Zn-Zr alloys by the LPSO structure is due to the low potential difference between the LPSO phase and matrix.

2. Experimental

2.1. Material preparation

The conventional ingot metallurgy process was employed to produce the as-cast Mg-15Gd-2Zn-0.39Zr alloy (denoted as Mg-Gd-Zn-Zr alloy for simplification). The composition of the Mg-Gd-Zn-Zr alloy was Gd-15, Zn-2.19, Zr-0.39, Al-0.0041, Si-0.0025, Fe-0.001, S-0.0043, and Mg-balanced in wt.%, which was analyzed using an inductive coupled plasma-atomic emission spectrometer (ICP-AES, X Series II).

Then the middle regions of the as-cast Mg-Gd-Zn-Zr alloys were cut into test coupons with the dimensions of $20 \times 20 \times 10$ mm. In order to obtain the LPSO structure, parts of specimens were solid solution heat-treatment at 773 K for 35 h, followed by immediate quenching in cold water [5] (denoted as T4-treatment). The electrochemical specimens were embedded in an epoxy resin leaving an exposed area of 4 cm^2 as working electrode surfaces. The other end of the specimens was connected to a copper wire to create an electrical connection. Before each experiment, all the specimens were wet ground to a 2000 grit-finish by a SiC paper gradually (for SEM and SKPFM observation, the specimen surface was polished to a 0.5 μm-finish with ethanol lubricant).

The test solution was a 3.5 wt% NaCl solution saturated with $Mg(OH)_2$, which was prepared by analytical grade reagents and deionized water. The salt solution saturated with $Mg(OH)_2$ shows a stable pH value of around 10.3 ensuring the reproducibility of the electrochemical experiments. Besides, as Mg metal dissolves quickly, it is quite easy to obtain a high local pH value at its surface. Therefore, the $Mg(OH)_2$ saturated solution represents the thin electrolyte layer adjacent to the magnesium alloy surface in NaCl solution to some extent.

In addition, in this study, a commercial AZ91D Mg alloy was also prepared for the comparison of the corrosion behavior between traditional Mg alloys and Mg-RE alloys.

2.2. Corrosion test

The corrosion rate of Mg-Gd-Zn-Zr alloy was evaluated by the hydrogen evolution experiment and potentiodynamic polarization test. A set of self-developed apparatus including a beaker, burette and funnel was used for hydrogen evolution experiment [54]. The temperature was kept constant at 30 ± 1 °C, controlled by a water bath. When hydrogen bubbles are produced due to corrosion, there will be a change in the solution height in the burette. The data can be used for the calculation of hydrogen evolution volume and the evaluation of the corrosion rate. In the experiment, the data were recorded continuously for 192 h. The hydrogen evolution measurements were repeated three times for each kind of alloy.

A standard three-electrode cell was used to carry out the potentiodynamic polarization tests by a Zahner Zennium electrochemical workstation, where a platinum plate was applied as the counter electrode, a saturated calomel electrode (SCE) as the reference electrode, and Mg alloy specimens were applied as the working electrode. Before polarization tests, the specimens were stabilized at open circuit potential (OCP) for 30 min to reach a steady state. Then, separate potentiodynamic scanning of the cathode and anode was carried out with a uniform scan rate of 0.333 mV s^{-1}. The cathode polarization curve started from OCP to −300 $mV_{vs.OCP}$, whereas, the anode potentiodynamic scan started from OCP till the current density exceeded 5 mA cm^{-2}. A constant test temperature of 30 ± 1 °C was maintained using a water bath. The potentiodynamic polarization tests were repeated at least three times.

2.3. Materials characterization

An X-ray diffraction system (XRD, PHILIPS, PW1700) with Cu K_α radiation ($\lambda = 1.5406$ Å, 30 mA, 40 kV) was employed to identify the composition of Mg-Gd-Zn-Zr alloys and the corrosion products after hydrogen evolution experiment. The MDI Jade 5.0 software was used to analyze the obtained XRD patterns. Meanwhile, the components of the corrosion product layer were measured by an electron probe micro analyzer (EPMA, SHIMADZU, 1610). The micrograph observation and component characterization of Mg-Gd-Zn-Zr alloys were carried out by a scanning electron microscope (SEM, PHILIPS, XL-30FG), equipped with an energy dispersive spectrometer (EDS). In order to reveal the microstructure of each phase in the Mg-Gd-Zn-Zr alloys, transmission electron microscopy (TEM, JEOL, JEM-2100F) and high-resolution scanning transmission electron microscopy (HRSTEM, FEI, Tecnai-F30), equipped with a high angle angular dark field (HAADF) detector were also used. The specimens for TEM observation were prepared by argon ion milling. The high-resolution transmission X-ray tomography (HRTXT, X radia, VersaXRM-500) was used to characterize the spatial three-dimensional microstructure of the alloys. Moreover, in order to analyze the micro-electrochemical behavior of Mg-Gd-Zn-Zr alloys, a scanning Kelvin probe force microscope (SKPFM, Bruker Corporation, Multimode 3D) was employed to monitor the localized potential distribution in the studied alloys. The results of SKPFM were treated by NanoScope Analysis software.

3. Results

3.1. Microstructure of Mg-Gd-Zn-Zr alloys

3.1.1. Microstructure characterization

Fig. 1 shows the XRD pattern of the as-cast alloys and T4-treated alloys (denoted as T4 alloys for simplification), respectively. Two phases are identified in the as-cast alloys, which are α-Mg matrix and β-$(Mg,Zn)_3Gd$ phase [25,40,41]. However, the β-$(Mg,Zn)_3Gd$ phase disappears after the T4-treatment. Instead, a new phase appears in the T4 alloy, which is the X-$Mg_{12}ZnGd$ phase [14,41,42].

SEM images in Fig. 2 provide a detailed description of the microstructure of the Mg-Gd-Zn-Zr alloys. It indicates that the as-cast alloy consists α-Mg matrix and fine-lamellae eutectic phase, in which β-$(Mg,Zn)_3Gd$ is the second phase. The eutectic compounds are network-shaped and distributed continuously at the grain boundaries. The microstructure of T4 alloy is composed of α-Mg solid solution and X phase, as well as a small number of particles uniformly dispersed in the grain, which are identified as Zn_xZr ($x = 1,2$) [55] by later EDS (the absence of this phase in the XRD pattern may be ascribed to its small amount). The X phases are also distributed at the grain boundaries, but in contrast to the eutectic phases, the shape of X phases in T4 alloys is block-like and the distribution is not continuous. It has been reported that the X phase in Mg-Gd-Zn alloys can not only precipitate from the supersaturated Mg matrix, but can also be transformed from the decomposition of the second phase during the heat-treatment [25,28]. Therefore, combining with the morphology of X phase and the XRD results, some of the elements in β phase dissolved into the matrix during T4-treatment, whereas, a new X phase transformed when the compositions and stacking orders were satisfied [30].

In order to have a deep understanding of the microstructure of each phase in Mg-Gd-Zn-Zr alloys, TEM as well as HRSTEM observations were made, as shown in Fig. 3. It can be seen in Fig. 3(a) that there is a lamellar structure displayed in the α-Mg matrix in the bright-field TEM images in as-cast alloys. Further observation by HAADF-STEM in Fig. 3(b) indicates that the dark lines in the Mg matrix are just stacking faults of heavy metals but not LPSO structure. The selected area electron diffraction (SAED) patterns of the β phase in as-cast Mg-Gd-Zn-Zr alloys indicates that the β phase does not have an LPSO structure neither, but a fcc structure with a lattice constant of a = 0.720 nm (Fig. 3 (c)). The electron beam is parallel to the [110] zone axis. Subsequently, the HAADF-STEM observation was used to identify the microstructure of T4 alloys, as can be seen in Fig. 3(e). On the contrary to as-cast alloys, the dark lines at the edge between the α-Mg and X phase present both stacking faults structure and 14H-LPSO structure, the latter of which may be ascribed to the precipitation of supersaturated Mg matrix. The SAED patterns of X phase in T4 alloys with the electron beam parallel to the $[1\bar{2}10]$ direction is shown in Fig. 3(f). An obvious 14H-type LPSO structure is recognized from the corresponding diffraction patterns [5,14,41]. The lattice constants are estimated to be a = 0.325 nm and c = 3.722 nm, respectively. In conclusion, there is no LPSO structure in the as-cast Mg-Gd-Zn-Zr alloys, whereas, the 14H-LPSO structure is obtained in T4 alloys by the heat-treatment. This result is consistent with that of Yamasaki [24], who declared no LPSO phases were observed in the conventional cast Mg96.5Zn1Gd2.5 ingots, and concluded that the formation of the LPSO phase was controlled by heat-treatment.

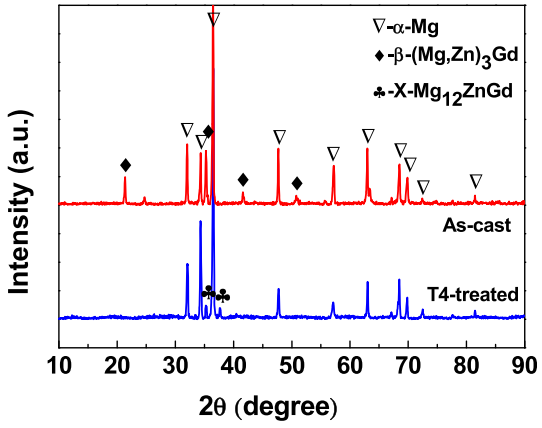

Fig. 1. XRD patterns of as-cast and T4-treated Mg-Gd-Zn-Zr alloys.

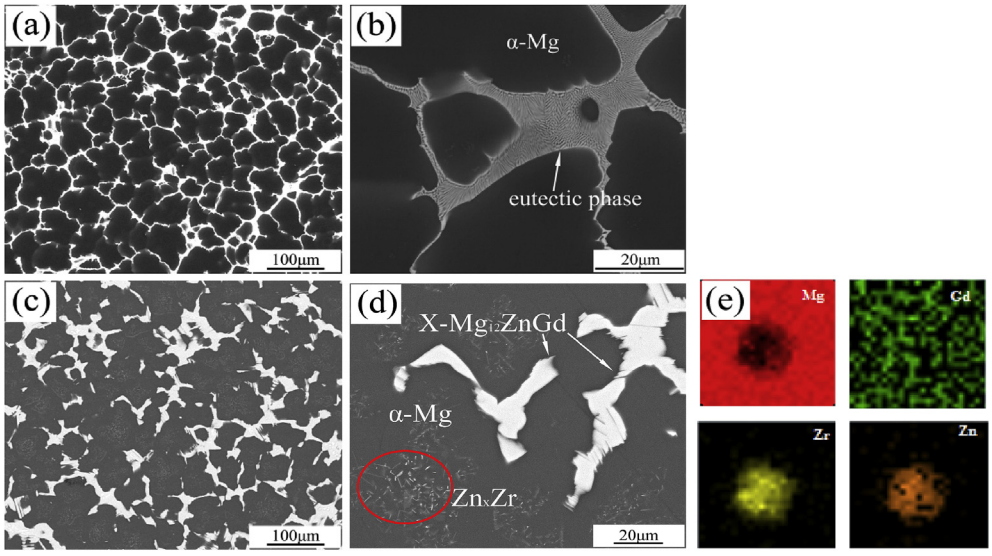

Fig. 2. (a,c) SEM images of as-cast and T4 alloys. (b,d) Enlarged SEM images of (a) and (c). (e) EDS mappings of one of the small particles inner the red circle in (d). (For interpretation of the references to colour in this figure legend, the reader is referred to the Web version of this article.)

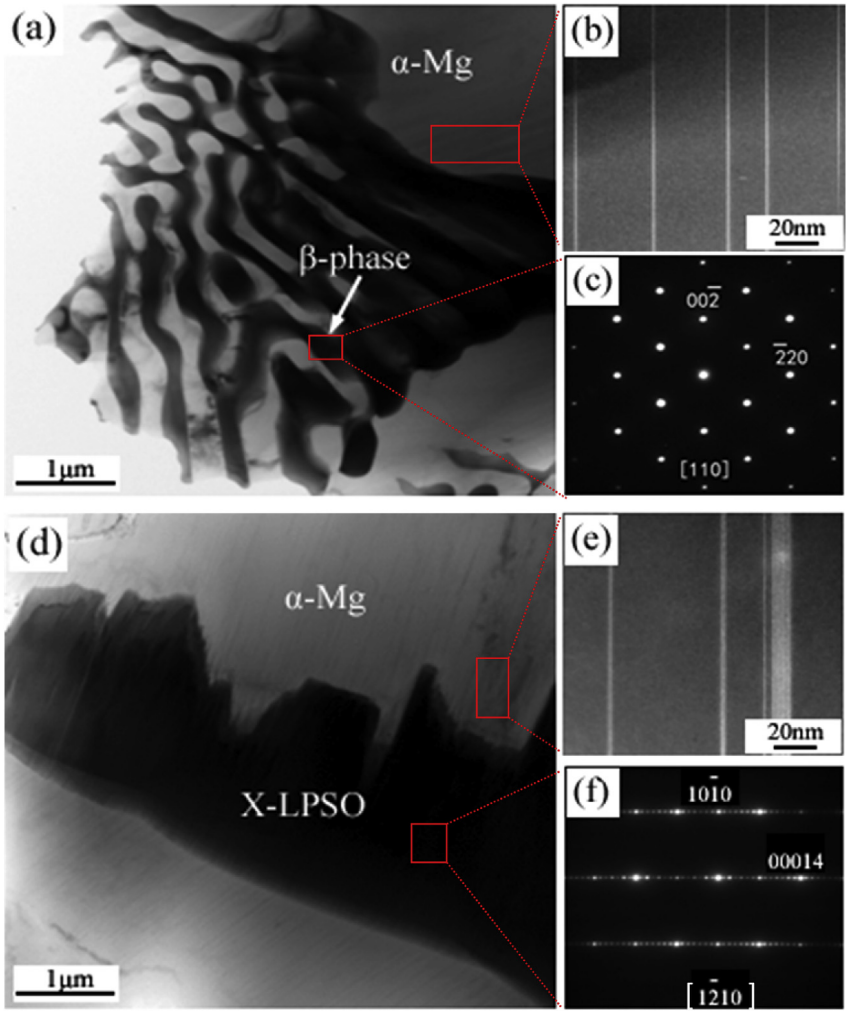

Fig. 3. Microstructure characterization of as-cast (above) and T4 (below) alloys. (a,d) Bright-field TEM micrographs. (b,e) HAADF-STEM images. (c,f) Selected area electron diffraction patterns of the second phases. The electron beam is parallel to [110] zone axis for as-cast alloys, and it is parallel to the [1$\bar{2}$10] direction for T4 alloys.

3.1.2. *Three-dimensional distribution*

In order to provide a visual and comprehensive characterization of the phases in three-dimensional space, HRTXT was used to characterize the dimensional distribution and calculate the volume fractions of each phase statistically. Results are shown in Fig. 4. The eutectic phases in as-cast Mg-Gd-Zn-Zr alloys present a dendritic distribution along the grain boundary throughout the whole alloy. It shows a continuous honeycomb-like network in the three-dimensional mapping. The volume fraction of the eutectic phase is extremely high, which reaches up to 42.8%. The LPSO phases

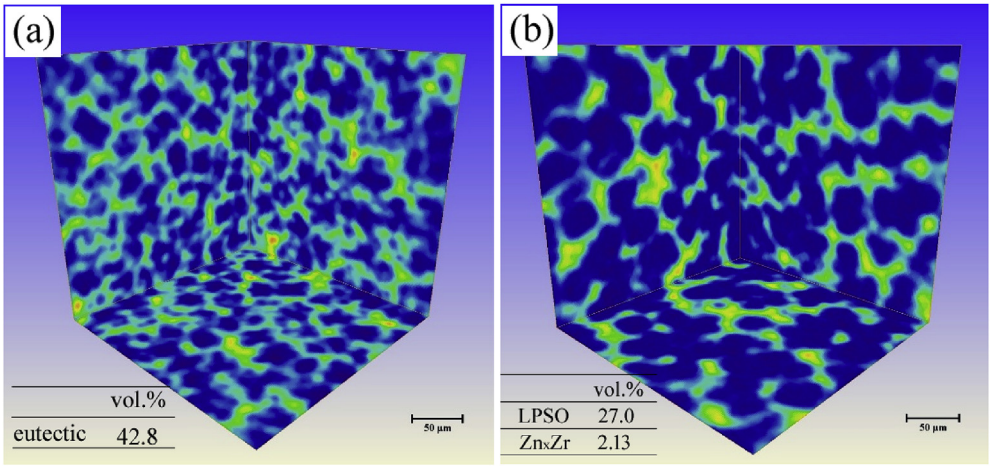

Fig. 4. Three-dimensional distribution images of (a) as-cast and (b) T4-treated Mg-Gd-Zn-Zr alloys by HRTXT.

exhibit a block-like shape and also distribute mainly around the grain boundary, but they are not connected with each other. The volume fraction of the LPSO phase is about 27%, which is much lower than that of the eutectic phase in as-cast alloys. As a result, the continuity of the LPSO phase is not as consecutive as eutectic phase, and it cannot present a network structure in the dimensional distribution. With regards to the volume fraction of Zn_xZr particles in T4 alloys, it occupies only 2.13% according to the statistics result of the apparatus.

3.2. Corrosion behavior of Mg-Gd-Zn-Zr alloys

3.2.1. Potentiodynamic polarization

Potentiodynamic polarization tests are used to evaluate the corrosion rate of Mg-Gd-Zn-Zr alloys (Fig. 5). It is clear that the as-cast alloy presents a passive characteristic in the anodic region, whereas the anodic curves of T4 alloy and AZ91D Mg alloy exhibit an active dissolution state. The detailed electrochemical parameters are summarized in Table 1. The corrosion current density (i_{corr}) of the as-cast alloy is lower than the other two alloys, which can be ascribed to the effect of the corrosion product film. In the initial stage, the production of $Mg(OH)_2$ and $Gd(OH)_3$ promotes the formation of a protective passive film on the surface, resulting in the passive anodic region and a low corrosion rate of the as-cast alloys [56]. The i_{corr} of the T4 alloys is three times higher than the as-cast alloys, which is due to the local potential distribution of the second phases and will be discussed in the later sections. Meanwhile, the potentiodynamic polarization curves and i_{corr} of the T4 alloy are almost identical to AZ91D Mg alloy, indicating a similar corrosion rate.

In addition, the formation of corrosion product film on the surface of as-cast alloy suppresses the hydrogen evolution reaction in the cathodic process. Therefore, according to the theory of mixed potential, the corrosion potential (E_{corr}) of the as-cast alloy is lower than T4 and AZ91D Mg alloy. Furthermore, the mechanism of hydrogen evolution process is still different between as-cast and T4 alloy. The Tafel slope of the as-cast alloy in the cathodic region equals to $-48\ mV\cdot dec^{-1}$, demonstrating an approximate chemical desorption reaction in the hydrogen evolution process [2,3]. While, it is $-110\ mV\cdot dec^{-1}$ for T4 alloy, implying an electrochemical desorption process [2,3].

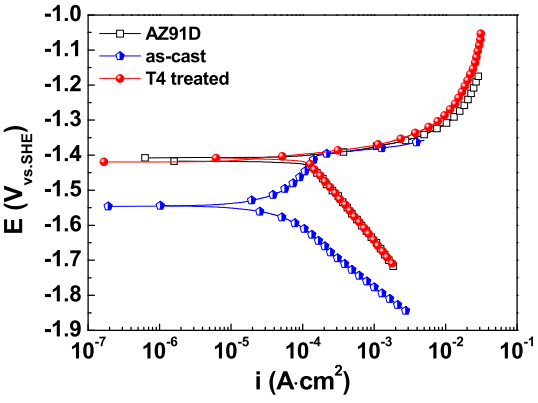

Fig. 5. Potentiodynamic polarization curves of Mg alloys.

Table 1
Electrochemical parameters obtained from potentiodynamic polarization curves in Fig. 5.

	AZ91D	As-cast	T4
E_{corr} (V)	−1.41	−1.54	−1.41
i_{corr} ($A\cdot cm^{-2}$)	1.12×10^{-4}	4.33×10^{-5}	1.16×10^{-4}
β_c ($mV\cdot dec$)	−108.48	−48.35	−102.19

3.2.2. Immersion test

The corrosion rate evaluated by potentiodynamic polarization is just a representation of the initial corrosion property. Therefore, the long-time immersion tests, as well as corrosion morphology and corrosion composition analyses, were carried out for the studied Mg-RE alloys to estimate the overall corrosion resistance. As the cathode electrochemical process of Mg alloys is mainly the hydrogen evolution reaction, the hydrogen evolution volume (HEV) can be used to evaluate the corrosion rate [57–59]. Hydrogen evolution rate (HER) is defined as the hydrogen evolution volume of a unit area specimen at a unit interval, and can be expressed as:

$$\mathrm{HER} = \frac{\Delta V}{S \times \Delta t} \quad (1)$$

where ΔV represents the hydrogen evolution volume at a certain time interval (mL), S is the specimen's area (cm^2), and Δt is the time interval (h).

Fig. 6 exhibits the HEV and HER of Mg-Gd-Zn-Zr alloys in $Mg(OH)_2$ saturated NaCl solution, as well as those of the commercial AZ91D Mg alloy for comparison. Obviously, the hydrogen evolution behaviors of as-cast and T4 alloys are quite different. For as-cast Mg-Gd-Zn-Zr alloys, the HEV and HER are $1\ mL\,cm^{-2}$ and $0.01\ mL\,cm^{-2}\,h^{-1}$ approximately during the initial 30 h, showing a relatively low value compared with T4 alloy, which is consistent with polarization results. However, subsequently, the HEV of as-cast alloy increases exponentially and linearly, and finally reaches up to an extremely high value of about $124\ mL\,cm^{-2}$ at the end of the experiment. Correspondingly, the HER increases linearly and

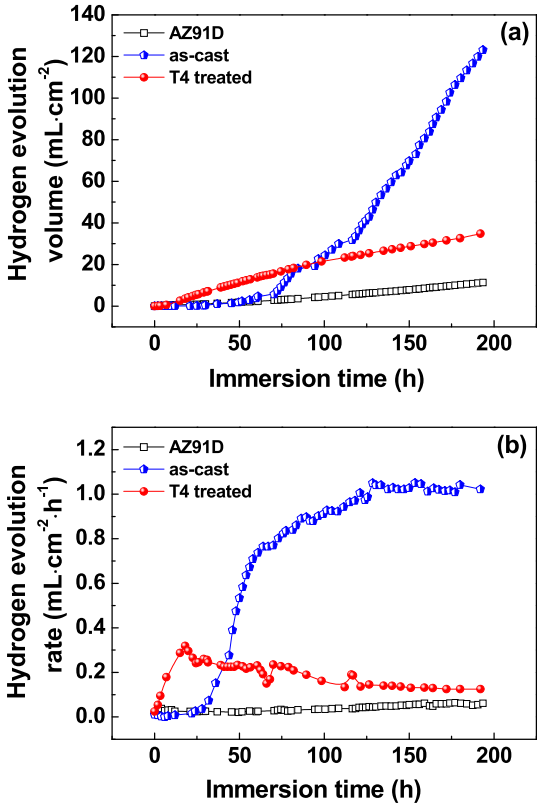

Fig. 6. Hydrogen evolution volume (a) and hydrogen evolution rate (b) of Mg alloys.

steeply until the 60th h, and finally, it does not change anymore and sustains a constant value of about 1.02 mL cm^{-2} h^{-1}. With regards to T4 alloys, the HEV is higher than the as-cast alloys in the initial stage. The HER of the T4 alloy shows a remarkable linear increase in the first 20 h. It reaches to the highest value of about 0.3 mL cm^{-2} h^{-1} at 20th h. Afterwards, the HEV of T4 alloy still increases as the immersion time prolongs but at a relatively lower speed. The final HEV was 34.8 mL cm^{-2} at the end of the immersion test. Correspondingly, the HER decreases gradually with a final value of about 0.12 mL cm^{-2} h^{-1}. As to the commercial AZ91D Mg alloy, both the HEV and HER increase slowly as immersion test prolongs with a final value of 11.3 mL cm^{-2} and 0.06 mL cm^{-2} h^{-1} respectively. According to the hydrogen evolution experiment results, it can be concluded that T4 alloys containing LPSO phase present a lower corrosion rate in the long-period corrosion process when compared with the as-cast alloys. Moreover, the corrosion rate of T4 alloys approaches to that of AZ91D Mg alloys.

After immersion experiments, the corrosion morphologies and compositions of corrosion product of Mg-Gd-Zn-Zr alloys were examined by SEM, XRD, and EPMA, respectively. The surface and cross sections of the corrosion morphologies show that the corrosion type is general corrosion and there is no difference between the as-cast and T4 alloys (Fig. 7 (a) and (b)). From the cross section micrographs in Fig. 7(c) and (d), it can be seen clearly that the corrosion product film is composed of a loose and laminated inner layer, and a compact outer layer. The corrosion product film provides a barrier for the penetration of corrosive ions to the metal surface. As a result, it hinders the corrosion process. Besides, the second phases also remain in the product film, implying that the matrix is a preferential dissolution phase and micro-galvanic corrosion is the main reason for the corrosion of Mg-Gd-Zn-Zr alloys. The second phases act as the cathode in micro-galvanic corrosion and accelerate the corrosion of α-Mg matrix in Mg-Gd-Zn-Zr alloys. On the other hand, the continuously distributed second phases also contribute to block the further propagation of corrosion until the dissolution or fall out of the second phases, as seen in Fig. 7(c) and (d). Thus, the second phases play important roles in the corrosion behavior of Mg-Gd-Zn-Zr alloys.

The compositions of the corrosion product were examined by EPMA and XRD, as shown in Figs. 8 and 9. The main elements presented in the corrosion product film are Mg, O, and Gd in both as-cast and T4 alloys. The XRD results also demonstrate there is no difference in the composition of the corrosion product film, which are Mg, $Mg(OH)_2$ and the remained second phases. In a word, the corrosion morphologies and corrosion products of both as-cast and T4 alloys are the same.

3.2.3. Corrosion initiation in mesoscale

Generally, the investigation of corrosion initiation is carried out by SEM observation after immersion experiment and the removal of corrosion product. However, the removal solution of corrosion product corrodes the eutectic phase and LPSO phase in Mg-Gd-Zn-Zr alloys, which disturbs the analysis of the initiation of corrosion. Therefore, an innovative method of HRSTEM observation was developed. The TEM foils were immersed in 3.5 wt% NaCl solution for 5 s, and then dried under an infrared lamp immediately for the HRSTEM observation. Fig. 10 exhibits the detailed HAADF-STEM images of the corrosion initiation in Mg-Gd-Zn-Zr alloys. A severe corrosion phenomenon occurs at the α-Mg matrix in the as-cast alloys in Fig. 10(a). The initiation of corrosion appears in the α-Mg matrix at the junction between the α-Mg matrix and β-$(Mg,Zn)_3Gd$ in the eutectic phase. Therefore, it is the effect of micro-galvanic between β phase and matrix that initiates the corrosion of the as-cast alloys. Correspondingly, in T4 alloys, the corrosion behavior is also observed in the α-Mg matrix at the boundary of the LPSO phase and matrix, whereas, the LPSO phase keeps immunity state, as shown in Fig. 10(b). It is also the LPSO phases in T4 alloys that promote the corrosion initiation of the α-Mg matrix in micro-

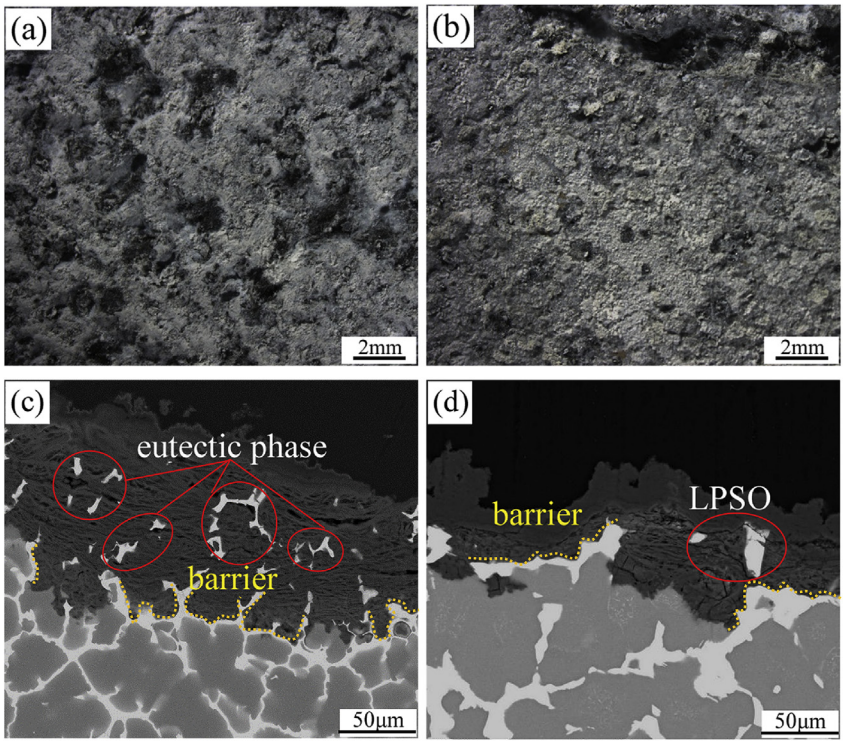

Fig. 7. Surface corrosion morphologies of (a) as-cast and (b) T4-treated Mg-Gd-Zn-Zr alloys, and cross-section corrosion morphologies of (c) as-cast and (d) T4 alloys.

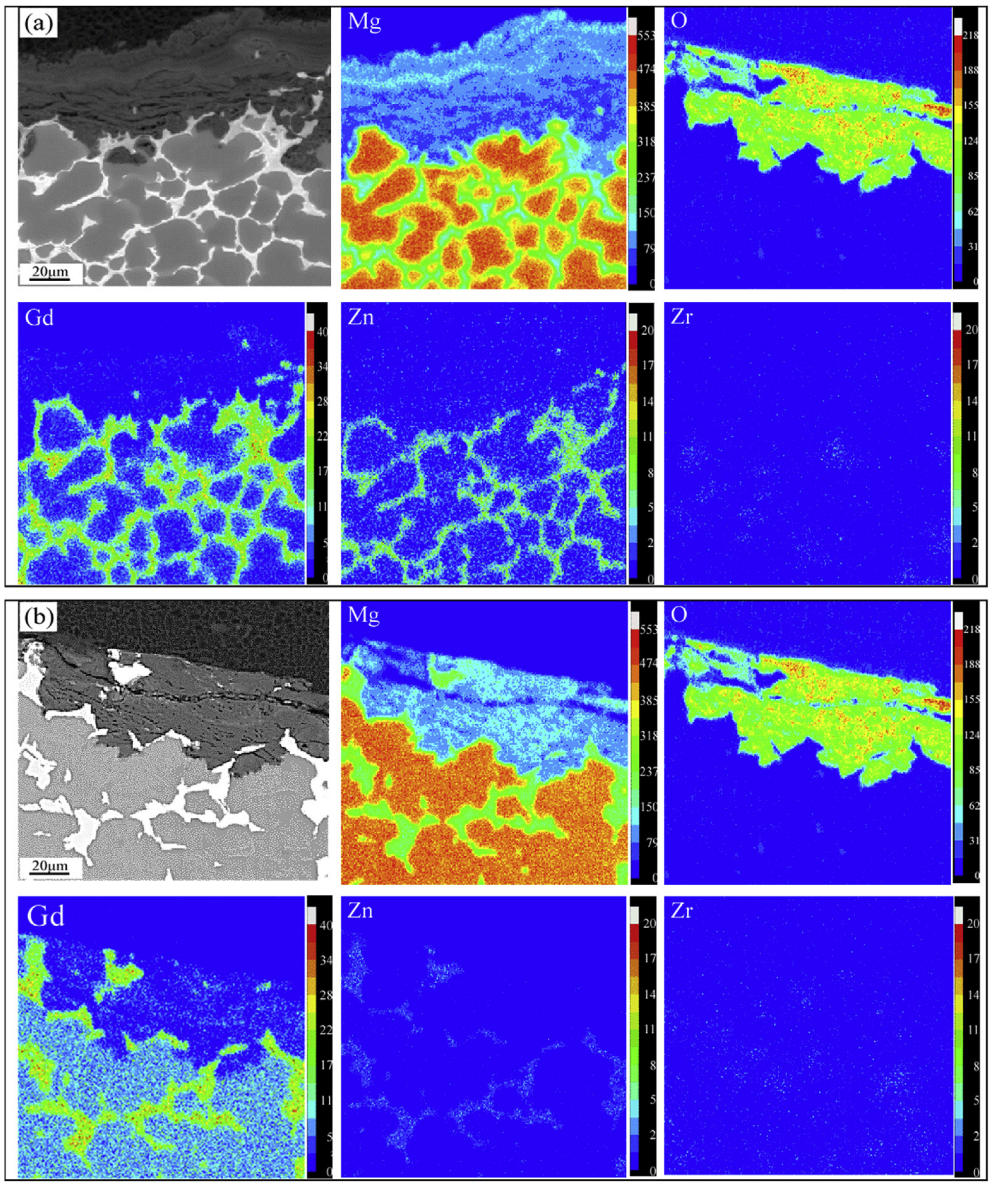

Fig. 8. Element maps of the corrosion product film in (a) as-cast and (b) T4 alloys by EPMA.

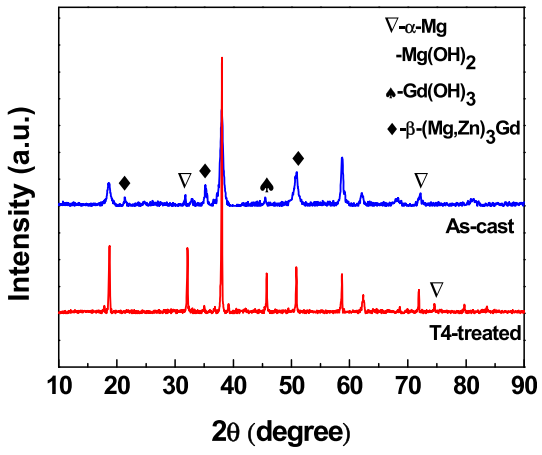

Fig. 9. XRD patterns of the corrosion product film in as-cast and T4-treated Mg-Gd-Zn-Zr alloys.

galvanic corrosion. In other words, the corrosion initiation of Mg-Gd-Zn-Zr alloys mainly originates from the micro-galvanic corrosion between the matrix and the second phases. The second phase, acting as a cathode, accelerates the corrosion progress of the α-Mg matrix and is vital in deciding the corrosion behavior of Mg-Gd-Zn-Zr alloys.

3.3. Local potential distribution in Mg-Gd-Zn-Zr alloy

SKPFM is a powerful tool for the investigation of micro-electrochemical behavior in corrosion research. Therefore, the micro-potential distribution of Mg-Gd-Zn-Zr alloys was studied by SKPFM and the data were acquired in two steps. First, the scanning height of the probe was set at 30 μm to obtain the relative height of surface morphology, and then, the probe scanned for the second time to acquire the potential information. The scan height was kept as 50 nm above the specimen surface depending on the surface height in the first scan. Fig. 11 shows the results of localized potential distribution between the α-Mg matrix and second phases by

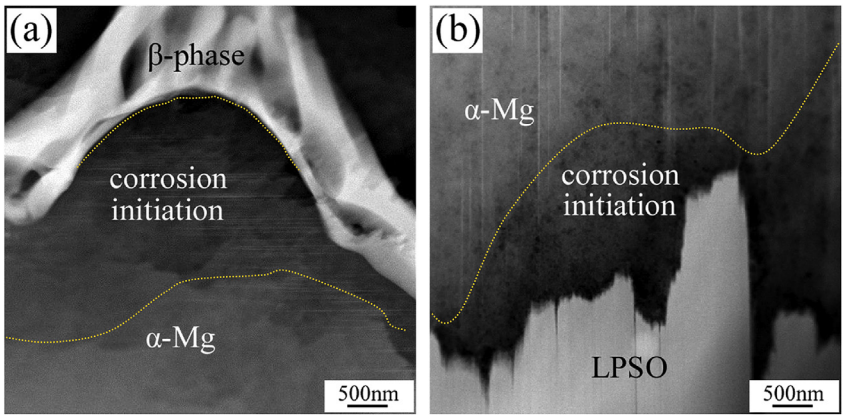

Fig. 10. HAADF-STEM images of (a) as-cast and (b) T4-treated Mg-Gd-Zn-Zr alloys after immersed in 3.5 wt% NaCl solution for 5 s.

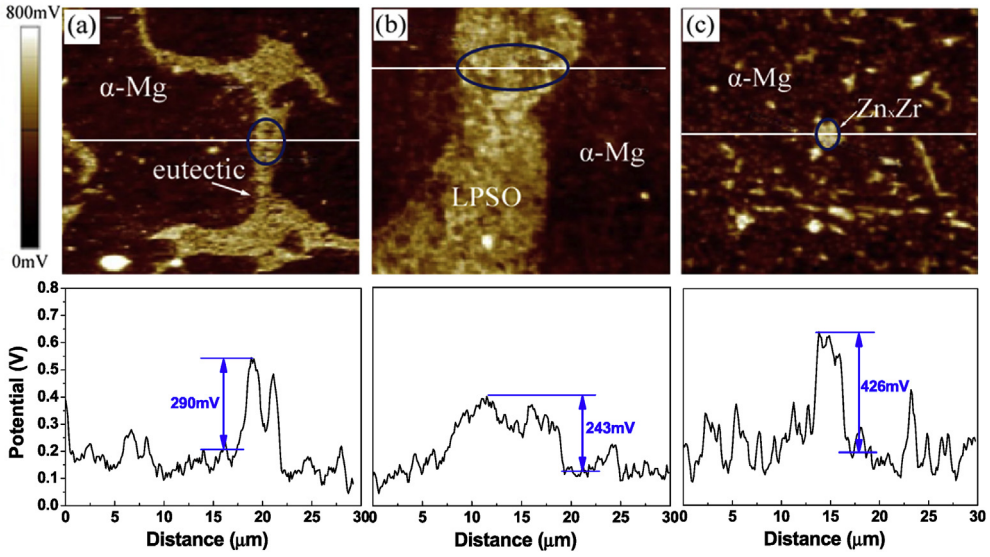

Fig. 11. SKPFM results of the local potential distribution between α-Mg matrix and (a) eutectic phase in as-cast alloys, (b) LPSO phase in T4 alloys, and (c) Zn_xZr particles in T4 alloys.

SKPFM. It reveals that the local potential of the eutectic phase, LPSO phase and Zn_xZr particles are all higher than the α-Mg matrix, indicating a substantial higher corrosion resistance. According to the line-profile results shown in Fig. 11(a), the potential difference between eutectic phase and the matrix is as high as 290 mV, implying the existence of micro-galvanic effect and the accelerated corrosion of α-Mg matrix by the eutectic phase. As to T4 alloys, the local potential of LPSO phase is still higher than the matrix, but with a relatively small potential difference of about 243 mV (as seen in Fig. 11(b)), indicating that the acceleration effect of micro-galvanic corrosion by the LPSO phase is relatively week. However, for the small amount of Zn_xZr particles, its relative potential is higher than other phases, indicating a noble nature of Zn_xZr, as shown in Fig. 11(c). The SKPFM results conform with the experimental phenomenon as observed in the SEM of corrosion product film and TEM of the corrosion initiation. It reveals the degree of micro-galvanic corrosion in Mg-Gd-Zn-Zr alloys quantitatively. The relative potential values reduce in the following order: Zn_xZr > eutectic phase > LPSO phase > α-Mg matrix. The LPSO phases exhibit a lower local potential compared with the eutectic phase, declaring a less degree of acceleration corrosion of α-Mg matrix in the micro-galvanic corrosion.

4. Discussion

Corrosion initiation observations by TEM (Fig. 10) and SKPFM results (Fig. 11) have illustrated that the micro-galvanic corrosion is the main corrosion mechanism for the studied Mg-RE alloys. Meanwhile, the intense corrosion product film in Fig. 7 also has an effect on the corrosion process. It has been commonly recognized that the second phase can act as a galvanic cathode and (or) serve as a barrier phase in the micro-galvanic corrosion process for Mg alloys [60–64]. Therefore, the corrosion behavior of as-cast alloys and T4 alloys are affected commonly by the acceleration effect of the second phase due to its high local potential, the barrier effect of a continuously distributed second phase, and the hinder effect of the corrosion product film.

In the initial stage, by deposition of $Mg(OH)_2$ and $Gd(OH)_3$, the corrosion product film acting as a barrier hinders the penetration of corrosive ion and further corrosion process. In addition, the eutectic phases with a 42.8% volume fraction present a consecutive cellular structure in three-dimension, which blocks the propagation of corrosion. As a result, the corrosion rate of the as-cast alloy is low during the initial stage. However, the Zn_xZr particles in T4 alloys induce a micro-galvanic corrosion in the initial stage due to their

high local potentials, which breaks the protectiveness of the corrosion product film. Moreover, the role of the LPSO phase in T4 alloys is entirely different from the eutectic phase in the as-cast alloys. There is no barrier phase effect due to the inconsecutive distribution of LPSO phase. On the contrary, the LPSO phases acting as the cathodic phases, promote the micro-galvanic corrosion of the matrix. Therefore, the corrosion rate of the T4 alloy is relatively higher than the as-cast Mg alloys during the initial stage.

As immersion time prolongs, a dramatic increase of corrosion rate of as-cast alloys occurred. On one hand, after a period of pregnant and propagation, the micro-galvanic corrosion between eutectic phase and Mg matrix breaks up the passivity of the corrosion product film. On the other hand, the eutectic phases fall off as the dissolution of Mg matrix, and consequently, the barrier effect of the second phase is reduced [17,41]; Instead, the cathodic phase effect of the eutectic phase evokes a severe micro-galvanic corrosion due to its high relative potential (290 mV). As a result, the corrosion rate of the as-cast alloy increases dramatically in the subsequent corrosion tests. Finally, under the acceleration effect of the micro-galvanic corrosion and the barrier effect of the corrosion product film, the as-cast alloys present a steady corrosion rate of about 1.02 mL cm^{-2} h^{-1}. However, at a prolonged immersion time, there is no variation in the role of second phases in the corrosion behavior of T4 alloys. It is still the cathodic phase effect of the second phases that promotes the micro-galvanic corrosion of the matrix. Therefore, the HER keeps a steady state throughout the whole experiment. Finally, with the benefit of the deposition of the corrosion product, the corrosion rate of T4 alloys decreases gradually [9,17,39] with a final value of about 0.12 mL cm^{-2} h^{-1}, which is similar to that of AZ91D Mg alloy (0.06 mL cm^{-2} h^{-1}).

It should be mentioned that the HER between as-cast alloys and T4 alloys differs a lot ultimately, which can be attributed to the difference in the acceleration effect of the second phases in micro-galvanic corrosion. As illustrated in Fig. 11, the local potential difference of the second phases is a reflection of the micro-galvanic acceleration effect to some extent. For as-cast alloys, the local potential of eutectic phase is 290 mV relative to Mg matrix, whereas, it reduces to 243 mV for LPSO phase due to the difference in chemical composition. When combined with the volume fraction results of the second phases in Fig. 4, the acceleration effect of the LPSO phase in micro-galvanic corrosion decreases significantly compared with eutectic phase. As for Zn_xZr particles, the little volume fraction (2.13%) and little size bring out little effect on micro-galvanic corrosion. The Zn_xZr particle should fall off during corrosion and can not have a permanent effect on the micro-galvanic corrosion. Therefore, the acceleration effect of the second phase in T4 alloys is mainly reflected in the presence of LPSO phases in the long-term corrosion process. As a result, the T4 alloys present an absolute lower corrosion rate than the as-cast alloy ultimately.

The schematic diagram of the corrosion mechanism of Mg-Gd-Zn-Zr alloys is displayed in Fig. 12. The parameters concerning the relationship between the corrosion rate and microstructure characteristic are summarized in Table 2. In summary, in the long-term corrosion process, the local potential and the volume fraction of the second phases determine the acceleration degree of micro-galvanic corrosion, and finally, play an important role in affecting the corrosion rate of Mg-Gd-Zn-Zr alloys. The LPSO phases possess a lower relative potential and volume fraction, and therefore, have a

Table 2
Summarization of the local potential and volume fraction of second phases concerning with the corrosion rate in Mg alloys.

Parameters	AZ91D Mg alloys	As-cast Mg-Gd-Zn alloys	T4 treated Mg-Gd-Zn alloys	
	β-$Mg_{17}Al_{12}$	Eutectic phase	X-LPSO	ZnZr
Local potential difference (mV)	180	290	243	426
Volume fractions (%)	/	42.8	27.0	2.13
Hydrogen evolution rate ($mL \cdot cm^{-2} \cdot h^{-1}$)	0.06	1.02	0.12	

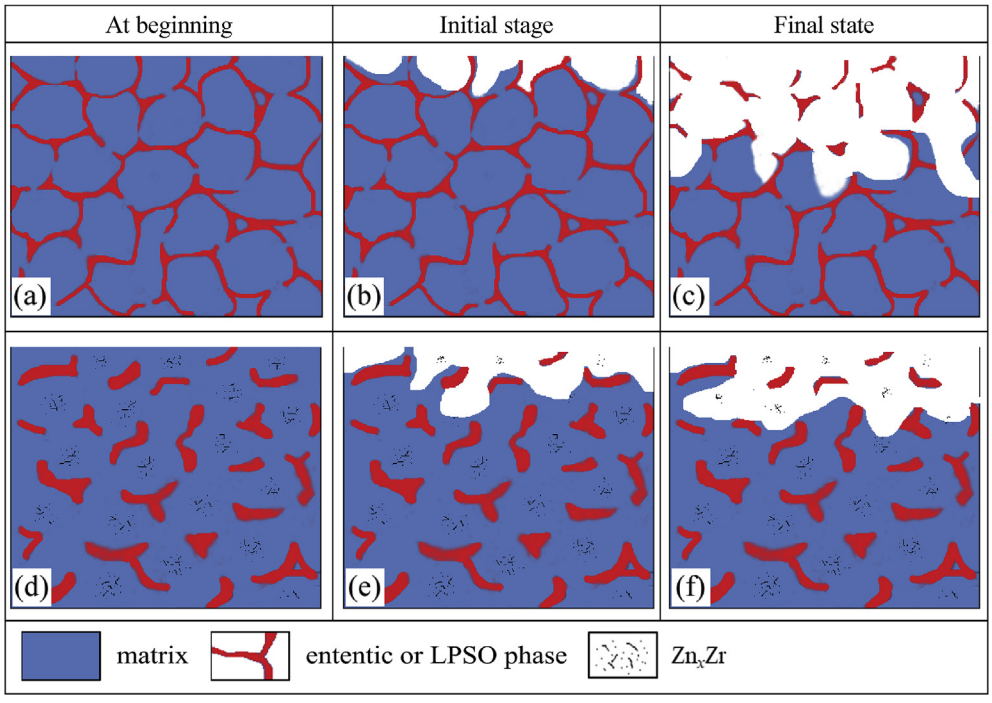

Fig. 12. Schematic diagrams of the corrosion mechanism of as-cast (a–c) and T4-treated (d–f) Mg-Gd-Zn-Zr alloys with immersion time prolongs.

crucial effect on the improvement of the corrosion resistance of the Mg-Gd-Zn-Zr alloys.

5. Conclusions

The as-cast alloy is composed of α-Mg matrix and β-$(Mg,Zn)_3Gd$ eutectic phase. The corrosion rate is low during the initial stage due to the barrier effect of eutectic phase and the corrosion product film, whereas, it increases dramatically subsequently because of the acceleration of the micro-galvanic corrosion by β phase. The hydrogen evolution rate is 1.02 mL cm^{-2} h^{-1} at the end of the experiment.

After T4-treatment, the β phase in the as-cast Mg-Gd-Zn-Zr alloys transforms into an X phase with a 14H-LPSO structure. The corrosion rate of the T4 alloy is determined by the acceleration effect of the LPSO phase in the micro-galvanic corrosion during the whole experiment. Therefore, the corrosion rate increases during the initial stage, whereas, it decreases gradually as immersion time prolongs due to the deposition of corrosion product film and the passivity of RE. Finally, T4 alloy presents a hydrogen evolution rate of about 0.12 mL cm^{-2} h^{-1}.

The corrosion rate of Mg-Gd-Zn-Zr alloys is mainly determined by the acceleration effect of the second phase in the micro-galvanic corrosion. LPSO phases possess a low potential and volume fraction, which reduce the acceleration degree of micro-galvanic corrosion. As a result, the corrosion resistance of Mg-Gd-Zn-Zr alloys improves significantly by the LPSO structure.

Acknowledgements

The authors are grateful to the financial support from the National Natural Science Foundation of China (Nos. 51531007, 51771050), the National program for the Young Top-notch Professionals, the Fundamental Research Funds for the Central Universities (N170205002).

Appendix A. Supplementary data

Supplementary data to this article can be found online at https://doi.org/10.1016/j.jallcom.2018.12.233.

References

[1] X.W. Yu, B. Jiang, J.J. He, B. Liu, F.S. Pan, Oxidation resistance of Mg-Y alloys at elevated temperatures and the protection performance of the oxide films, J. Alloys Compd. 749 (2018) 1054–1062.
[2] G.L. Song, A. Atrens, Understanding magnesium corrosion—a framework for improved alloy performance, Adv. Eng. Mater. 5 (2003) 837–858.
[3] G.L. Song, A. Atrens, Corrosion mechanisms of magnesium alloys, Adv. Eng. Mater. 1 (1999) 11–33.
[4] Y.J. Wu, L.M. Peng, X.Q. Zeng, formation of a novel X phase in Mg-Gd-Zn-Zr alloy [C], Mater. Sci. Forum (2010) 623–626.
[5] Y.J. Wu, X.Q. Zeng, D.L. Lin, L.M. Peng, W.J. Ding, The microstructure evolution with lamellar 14H-type LPSO structure in an $Mg_{96.5}Gd_{2.5}Zn_1$ alloy during solid solution heat treatment at 773 K, J. Alloys Compd. 477 (2009) 193–197.
[6] R.C. Zeng, L. Sun, Y.F. Zheng, H.Z. Cui, E.H. Han, Corrosion and characterization of dual phase Mg-Li-Ca alloy in Hank's solution: the influence of microstructural features, Corros. Sci. 79 (2014) 69–82.
[7] J. Jiang, Y. Wang, G. Chen, J. Liu, Y. Li, S. Luo, Comparison of mechanical properties and microstructure of AZ91D alloy motorcycle wheels formed by die casting and double control forming, Mater. Des. 40 (2012) 541–549.
[8] F. Wu, S. Zhang, Z. Tao, Corrosion behavior of 3C magnesium alloys in simulated sweat solution, Mater. Corros. 62 (2011) 234–239.
[9] J.F. Wang, R.P. Lu, W.W. Wei, X.F. Huang, F.S. Pan, Effect of long period stacking ordered (LPSO) structure on the damping capacities of Mg-Cu-Mn-Zn-Y alloys, J. Alloys Compd. 537 (2012) 1–5.
[10] F.R. Cao, B.J. Zhou, X. Ding, J. Zhang, G.M. Xu, Mechanical properties and microstructural evolution in a superlight Mg-7.28Li-2.19Al-0.091Y alloy fabricated by rolling, J. Alloys Compd. 745 (2018) 436–445.
[11] F.S. Pan, M.B. Yang, X.H. Chen, A review on casting magnesium alloys: modification of commercial alloys and development of new alloys, J. Mater. Sci. Technol. 32 (2016) 1211–1221.
[12] J. Xu, B. Guan, H.H. Yu, X.Z. Cao, Y.C. Xin, Q. Liu, Effect of twin boundary-dislocation- solute interaction on detwinning in a Mg-3Al-1Zn alloy, J. Mater. Sci. Technol. 32 (2016) 1239–1244.
[13] S. Izumi, M. Yamasaki, Y. Kawamura, Relation between corrosion behavior and microstructure of Mg-Zn-Y alloys prepared by rapid solidification at various cooling rates, Corros. Sci. 51 (2009) 395–402.
[14] A. Srinivasan, C. Blawert, Y. Huang, C.L. Mendis, K.U. Kainer, N. Hort, Corrosion behavior of Mg-Gd-Zn based alloys in aqueous NaCl solution, J. Magn. Alloys 2 (2014) 245–256.
[15] C.Q. Li, D.K. Xu, Z.R. Zeng, B.J. Wang, L.Y. Sheng, X.B. Chen, E.H. Han, Effect of volume fraction of LPSO phases on corrosion and mechanical properties of Mg-Zn-Y alloys, Mater. Des. 121 (2017) 430–441.
[16] N. Birbilis, M.A. Easton, A.D. Sudholz, S.M. Zhu, M.A. Gibson, On the corrosion of binary magnesium-rare earth alloys, Corros. Sci. 51 (2009) 683–689.
[17] F.M. Lu, A.B. Ma, J.H. Jiang, Y. Guo, D.H. Yang, D. Song, J.Q. Chen, Significantly improved corrosion resistance of heat-treated Mg-Al-Gd alloy containing profuse needle-like precipitates within grains, Corros. Sci. 94 (2015) 171–178.
[18] X. Xia, J.F. Nie, C.H.J. Davies, W.N. Tang, S.W. Xu, N. Birbilis, An artificial neural net-work for predicting corrosion rate and hardness of magnesium alloys, Mater. Des. 90 (2016) 1034–1043.
[19] H.C. Pan, F.H. Wang, L. Jin, M.L. Feng, J. Dong, Mechanical behavior and microstructure evolution of a rolled magnesium alloy AZ31B under low stress triaxiality, J. Mater. Sci. Technol. 32 (2016) 1282–1288.
[20] K. Hagihara, A. Kinoshita, Y. Sugino, M. Yamasaki, Y. Kawamura, H.Y. Yasud, Y. Umakoshi, Effect of long-period stacking ordered phase on mechanical properties of $Mg_{97}Zn_1Y_2$ extruded alloy, Acta Mater. 58 (2010) 6282–6293.
[21] G. Garcés, E. Oñorbe, F. Dobes, Effect of microstructure on creep behaviour of cast Mg_{97} Y_2Zn_1 (at.%) alloy, Mater. Sci. Eng. A 539 (2012) 48–55.
[22] E. Oñorbe, G. Garcés, P. Pérez, Effect of the LPSO volume fraction on the microstructure and mechanical properties of Mg-Y_2X-Zn alloys, J. Mater. Sci. 47 (2012) 1085–1093.
[23] Z.L. He, P.H. Fu, Y. Wang, X. Xu, W. Ding, High cycle fatigue behavior of as-cast $Mg_{96.34}Gd_{2.5}Zn_1Zr_{0.16}$ alloy fabricated by semi-continuous casting, Mater. Sci. Eng. A 587 (2013) 72–78.
[24] M. Yamasaki, T. Anan, S. Yoshimoto, Mechanical properties of warm-extruded Mg-Zn-Gd alloy with coherent 14H long periodic stacking ordered structure precipitate, Scr. Mater. 53 (2005) 799–803.
[25] D.K. Xu, E.H. Han, Y.B. Xu, Effect of long-period stacking ordered phase on microstructure, mechanical property and corrosion resistance of Mg alloys: a review, Prog. Nat. Sci. Mater. Int. 26 (2016) 117–128.
[26] I. Stulikova, B. Smola, J. Cizek, T. Kekule, O. Melikhova, H. Kudrnova, Natural and artificial aging in Mg-Gd binary alloys, J. Alloys Compd. 738 (2018) 173–181.
[27] Y. Li, W.L. Xiao, F. Wang, T. Hu, C.L. Ma, The roles of long period stacking ordered structure and Zn solute in the hot deformation behavior of Mg-Gd-Zn alloys, J. Alloys Compd. 745 (2018) 33–43.
[28] Q.M. Peng, X.L. Hou, L.D. Wang, Y.M. Wu, Z.Y. Cao, L.M. Wang, Microstructure and mechanical properties of high performance Mg-Gd based alloys, Mater. Des. 30 (2009) 292–296.
[29] L. Yang, Y. Huang, Q. Peng, F. Feyerabend, K.U. Kainer, R. Willumeit, N. Hort, Mechanical and corrosion properties of binary Mg-Dy alloys for medical applications, Mater. Sci. Eng. B 176 (2011) 1827–1834.
[30] S. Zhang, G.Y. Yuan, C. Lu, W.J. Ding, The relationship between $(Mg,Zn)_3RE$ phase and 14H-LPSO phase in Mg-Gd-Y-Zn-Zr alloys solidified at different cooling rates, J. Alloys Compd. 509 (2011) 3515–3521.
[31] M. Yamasaki, M. Sasaki, M. Nishijima, K. Hiraga, Y. Kawamura, Formation of 14H long period stacking ordered structure and profuse stacking faults in Mg-Zn-Gd alloys during isothermal aging at high temperature, Acta Mater. 55 (2007) 6798–6805.
[32] Y. Kawamura, K. Hayashi, A. Inoue, Rapidly solidified powder metallurgy $Mg_{97}Zn_1Y_2$ alloys with excellent tensile yield strength above 600 MPa, Mater. Trans. 42 (2001) 1172–1176.
[33] E. Abe, Y. Kawamura, K. Hayashi, Long-period ordered structure in a high-strength nanocrystalline Mg-1Zn-2Y alloy studied by atomic-resolution Z-contrast STEM, Acta Mater. 50 (2002) 3845–3857.
[34] Y. Kawamura, T. Kasahara, S. Izumi, Elevated temperature $Mg_{97}Y_2Cu_1$ alloy with long period ordered structure, Scr. Mater. 55 (2006) 453–456.
[35] Y. Kawamura, M. Yamasaki, Formation and mechanical properties of Mg-Zn1-RE2 alloys with long-period stacking ordered structure, Mater. Trans. 48 (2007) 2986–2992.
[36] Z.M. Li, D.Q. Wan, Y. Huang, S.T. Ye, Y.L. Hu, Characterization of a $Mg_{95.5}Zn_{1.5}Y_3$ alloy both containing W phase and LPSO phase with or without heat treatment, J. Magn. Alloys 5 (2017) 217–224.
[37] M. Yamasaki, S. Izumi, Y. Kawamura, H. Habazaki, Corrosion and passivation behavior of Mg-Zn-Y-Al alloys prepared by cooling rate-controlled solidification, Appl. Surf. Sci. 257 (2011) 8258–8267.
[38] X.B. Zhang, Z.X. Ba, Z.Z. Wang, Y.J. Wu, Y.J. Xue, Effect of LPSO structure on mechanical properties and corrosion behavior of as-extruded GZ51K magnesium alloy, Mater. Lett. 163 (2016) 250–253.
[39] X.B. Zhang, Q. Wang, F.B. Chen, Y.J. Wu, Z.Z. Wang, Q. Wang, Relation between LPSO structure and biocorrosion behavior of biodegradable GZ51K alloy, Mater. Lett. 138 (2015) 212–215.
[40] X.B. Zhang, Z.X. Ba, Z.Z. Wang, Y.J. Xue, Microstructures and corrosion behavior of biodegradable Mg-6Gd-xZn-0.4Zr alloys with and without long

period stacking ordered structure, Corros. Sci. 105 (2016) 68–77.
[41] A. Srinivasan, Y. Huang, C.L. Mendis, C. Blawert, K.U. Kainer, N. Hort, Investigations on microstructures, mechanical and corrosion properties of Mg-Gd-Zn alloys, Mater. Sci. Eng. A 595 (2014) 224–234.
[42] J.F. Wang, W.Y. Jiang, Y. Ma, Y. Li, S. Huang, Substantial corrosion resistance improvement in heat-treated Mg-Gd-Zn alloys with a long period stacking ordered structure, Mater. Chem. Phys. 203 (2018) 352–361.
[43] X.B. Zhang, Y.J. Wu, Y.J. Xue, Z.Z. Wang, L. Yang, Biocorrosion behavior and cytotoxicity of a Mg-Gd-Zn-Zr alloy with long period stacking ordered structure, Mater. Lett. 86 (2012) 42–45.
[44] X.B. Zhang, Z.X. Ba, Q. Wang, Y.J. Wu, Z.Z. Wang, Q. Wang, Uniform corrosion behavior of GZ51K alloy with long period stacking ordered structure for biomedical application, Corros. Sci. 88 (2014) 1–5.
[45] P. Pérez, E. Onofre, S. Cabeza, I. Llorente, J.A. del Valle, M.C. García-Alonso, P. Adeva, Corrosion behaviour of Mg-Zn-Y-Mischmetal alloys in phosphate buffer saline solution, Corros. Sci. 69 (2013) 226–235.
[46] J.S. Zhang, J.D. Xu, W.L. Cheng, C.J. Chen, J.J. Kang, Corrosion behavior of Mg-Zn-Y alloy with long-period stacking ordered structures, J. Mater. Sci. Technol. 28 (2012) 1157–1162.
[47] J.Y. Zhang, M. Xu, X.Y. Teng, M. Zuo, Effect of Gd addition on microstructure and corrosion behaviors of Mg-Zn-Y alloy, J. Magn. Alloys 4 (2016) 319–325.
[48] J.W. Chang, X.W. Guo, P.H. Fu, L.M. Peng, W.J. Ding, Effect of heat treatment on corrosion and electrochemical behavior of Mg-3Nd-0.2Zn-0.4Zr (wt.%) alloy, Electrochim. Acta 52 (2007) 3160–3167.
[49] G.L. Bi, J. Jiang, F. Zhang, D.Q. Fang, Y.D. Li, Y. Ma, Y. Hao, Microstructure evolution and corrosion properties of Mg-Dy-Zn alloy during cooling after solution treatment, J. Rare Earths 34 (2016) 931–937.
[50] X. Zhao, L.L. Shi, J. Xu, Mg-Zn-Y alloys with long-period stacking ordered structure: in vitro assessments of biodegradation behavior, Mater. Sci. Eng. C 33 (2013) 3627–3637.
[51] Q.M. Peng, J.X. Guo, H. Fu, X.C. Cai, Y.N. Wang, B.Z. Liu, Z.G. Xu, Degradation behavior of Mg-based biomaterials containing different long-period stacking ordered phases, Sci. Rep. 4 (2014) 3620.
[52] J.F. Wang, Y.Y. Wei, S.F. Guo, S. Huang, X.E. Zhou, F.S. Pan, The Y-doped MgZnCa alloys with ultrahigh specific strength and good corrosion resistance in simulated body fluid, Mater. Lett. 81 (2012) 112–114.
[53] D. Wang, J.S. Zhang, J.D. Xu, Z.L. Zhao, W.L. Cheng, C.X. Xu, Microstructure and corrosion behavior of Mg-Zn-Y-Al alloys with long-period stacking ordered structures, J. Magn. Alloys 2 (2014) 78–84.
[54] X.P. Lu, Y.Y. Chen, C.Y. Zhang, T. Zhang, B.X. Yu, H.B. Xu, F.H. Wang, Formation mechanism and corrosion performance of phosphate conversion coatings on AZ91 and Mg-Gd-Y-Zr alloy, J. Electrochem. Soc. 165 (2018) C601–C607.
[55] J.H. Li, J. Barrirero, G. Sha, H. Aboulfadl, F. Mücklich, P. Schumacher, Precipitation hardening of an Mg-5Zn-2Gd-0.4Zr (wt. %) alloy, Acta Mater. 108 (2016) 207–218.
[56] X.W. Guo, J.W. Chang, S.M. He, W.J. Ding, X. Wang, Investigation of corrosion behaviors of Mg-6Gd-3Y-0.4Zr alloy in NaCl aqueous solutions, Electrochim. Acta 52 (2007) 2570–2579.
[57] K. Schlüter, Z.M. Shi, C. Zamponi, F.Y. Cao, E. Quandt, A. Atrens, Corrosion performance and mechanical properties of sputter-deposited MgY and MgGd alloys, Corros. Sci. 78 (2014) 43–54.
[58] N.N. Aung, W. Zhou, Effect of grain size and twins on corrosion behaviour of AZ31B magnesium alloy, Corros. Sci. 52 (2010) 589–594.
[59] Z.M. Shi, A. Atrens, An innovative specimen configuration for the study of Mg corrosion, Corros. Sci. 53 (2011) 226–246.
[60] G.L. Song, Corrosion electrochemistry of magnesium (Mg) and its alloys [M], Corr. Magn. Alloys (2011) 3–65.
[61] O. Lunder, J.E. Lein, T.K. Aune, K. Nisancioglu, The role of $Mg_{17}Al_{12}$ phase in the corrosion of Mg alloy AZ91, Corrosion 45 (1989) 741–748.
[62] M.C. Zhao, M. Liu, G.L. Song, A. Atrens, Influence of the β-phase morphology on the corrosion of the Mg alloy AZ91, Corros. Sci. 50 (2008) 1939–1953.
[63] Y.J. Ko, C.D. Yim, J.D. Lim, K.S. Shin, Effect of $Mg_{17}Al_{12}$ precipitate on corrosion behavior of AZ91D magnesium alloy, Mater. Sci. Forum 419 (2003) 851–856.
[64] W. Zhou, T. Shen, N.N. Aung, Effect of heat treatment on corrosion behaviour of magnesium alloy AZ91D in simulated body fluid, Corros. Sci. 52 (2010) 1035–1041.